Article

The Use of C-/X-Band Time-Gapped SAR Data and Geotechnical Models for the Study of Shanghai's Ocean-Reclaimed Lands through the SBAS-DInSAR Technique

Antonio Pepe [1], Manuela Bonano [1], Qing Zhao [2,3,4,*], Tianliang Yang [5,6] and Hanmei Wang [5,6]

[1]   Institute for Electromagnetic Sensing of the Environment, Italian National Research Council,
     Via Diocleziano 328, Napoli 80124, Italy; pepe.a@irea.cnr.it (A.P.); bonano.m@irea.cnr.it (M.B.)
[2]   Key Laboratory of Geographical Information Science, Ministry of Education, East China Normal University,
     Shanghai 200241, China
[3]   School of Geographic Sciences, East China Normal University, Shanghai 200241, China
[4]   Joint Laboratory for Environmental Remote Sensing and Data Assimilation, East China Normal University,
     Shanghai 200062, China
[5]   Key Laboratory of Land Subsidence Monitoring and Prevention, Ministry of Land and Resources,
     Shanghai 200072, China; sigs_ytl@163.com (T.Y.); hanmeiw@163.com (H.W.)
[6]   Shanghai Institute of Geological Survey, Shanghai 200072, China
* Correspondence: qzhao@geo.ecnu.edu.cn; Tel.: +86-21-6222-4459

Abstract: In this work, we investigate the temporal evolution of ground deformation affecting the ocean-reclaimed lands of the Shanghai (China) megacity, from 2007 to 2016, by applying the Differential Synthetic Aperture Radar Interferometry (DInSAR) technique known as the Small BAseline Subset (SBAS) algorithm. For the analysis, we exploited two sets of non-time-overlapped synthetic aperture radar (SAR) data, acquired from 2007 to 2010, by the ASAR/ENVISAT (C-band) instrument, and from 2014 to 2016 by the X-band COSMO-SkyMed (CSK) sensors. The long time gap (of about three years) existing between the available C- and X-band datasets made the generation of unique displacement time-series more difficult. Nonetheless, this problem was successfully solved by benefiting from knowledge of time-dependent geotechnical models, which describe the temporal evolution of the expected deformation affecting Shanghai's ocean-reclaimed platforms. The combined ENVISAT/CSK (vertical) deformation time-series were analyzed to gain insight into the future evolution of displacement signals within the investigated area. As an outcome, we find that ocean-reclaimed lands in Shanghai experienced, between 2007 and 2016, average cumulative (vertical) displacements extending down to 25 centimeters.

1. Introduction

A feasible measure for resolving issues of land scarcity in highly populated coastal area cities or lowland countries is to reclaim land from the sea. For instance, The Netherlands has been reclaiming land since the sixteenth century, and, nowadays, one-third of their territory lies at heights lower than the mean sea level [1]. The Changi Airport in Singapore, the Honk Hong International Airport in China, the Kansai Airport in Japan, and the New Doha International Airport in Qatar, are all examples of public infrastructure built on reclaimed, or partially reclaimed, lands [2–7]. Reclaimed platforms can, however, be seriously affected by settlements, which may cause severe damage to buildings, highways,

airport runways, harbors, and underground facilities, thus, also resulting in a possible decrease in the height of sea walls. In particular, in China, about 1600 km^2 of new territories were reclaimed from 2002 to 2011 [8–11]. One of the largest reclamation projects in China is the plan approved in Lingang New City (new name, Nanhui New City), which is a district of the Shanghai megacity (see Figure 1), under which about 130 km^2 of land were reclaimed from the sea from 2003 to 2006. The reclamation project is currently in progress, and there are plans to recover about 1000 km^2 of new lands from the Yangtze River by the end of 2020 [10].
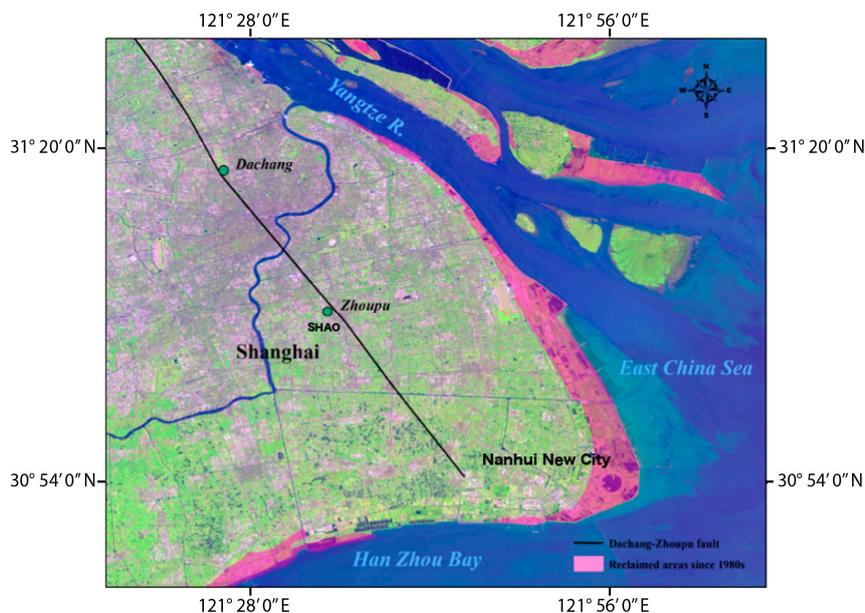

Figure 1. Landsat 8 image collected on 3 August 2015, which shows the city of Shanghai and its reclaimed coastal areas (since the 1980s) in Nanhui New City. Ocean-reclaimed areas are represented in pink and the black line identifies the Dachang–Zhoupu fault.

Over the past few years, the coastal area of Lingang New City, which extends for about 300 km^2 (45% of which was reclaimed from intertidal wetlands), has been subjected to broad modifications in its geomorphology and urban environment. Due to land reclamation, two main inherent problems have arisen: (i) liquefaction; and (ii) ground settlements, both of which are responsible for serious failures and damage to infrastructures of reclaimed foundations [12–14]. Results of geotechnical analyses have revealed that such a settlement usually continues over the entire reclamation facility lifetime. Temporal evolution of settlements can be distinguished in a primary consolidation phase of alluvial deposits, in a long-term creep (secondary compression stage) of the alluvial deposits beneath the reclamation, and, finally, in a creep within the reclamation fill [14]. These settlements may occur during and after foundation construction, and, when not correctly predicted, can cause delays and a considerable increase in costs of the whole reclamation project. Ground settlement of reclaimed coastal areas in Shanghai, which is caused by over-pumping groundwater and consolidation of dredger fills and alluvial deposits, have already been observed and reported in the literature [15–20]. In particular, field measurements indicate that ground settlement of the reclaimed foundations occurred during the construction of Lingang New City in Shanghai. Average cumulative (vertical) deformation values, ranging between 25 and 75 mm, in the six-year period from 2001 to 2006, corresponding to average annual rates ranging between 5 and 15 mm/year, have been measured [16]. Laboratory tests, based on the principles of the consolidation theory [21], were performed, taking into account dredger fill type (alluvial deposits thickness, soil composition, and water content) and other engineering parameters, which also predict that such a residual settlement will continue over future years, but with decreasing annual rates.

Within this framework, the well-established remote sensing technique, known as Differential Synthetic Aperture Radar (SAR) Interferometry (DInSAR) [22–25], can play a strategic role in the detection and monitoring of ongoing surface deformation signals at a large spatial scale. Over the past fifteen years, several DInSAR techniques aimed at investigating the time evolution of ground displacements have been proposed [26–31]. Two families of DInSAR methods broadly exist today, Persistent Scatterers (PS) [26,27] and Small Baseline (SB) techniques [28–30]. A well-known approach belonging to the class of SB techniques is the Small BAseline Subset (SBAS) [28] algorithm. It relies on the least-squares (LS) inversion of a suitably selected sequence of small baseline (SB) interferograms through the singular value decomposition (SVD) method [32]. Over recent years, DInSAR techniques have been widely applied to monitor deformation phenomena caused by several natural and anthropogenic hazards, including landslides [33,34], ground failures due to tunneling excavations [35,36], and terrain consolidation and land-subsidence of river deltas [37–39].

In this work, we investigate the deformation phenomena that affect the coastal area of the Shanghai megacity. Our study is based on the application of the SBAS-DInSAR technique to two sets of SAR images, collected by the C-band ASAR/ENVISAT sensor, and by the X-band COSMO-SkyMed (CSK) SAR constellation sensors. The processed SAR data span the entire time interval between 26 February 2007 and 18 March 2016. Due to the lack of a systematic acquisition plan of SAR data over the investigated area, there is a significant temporal gap (of about three years) between the available ASAR/ENVISAT and CSK data frames. As a matter of fact, over the past few years, satellite radar platforms have not regularly imaged the southeastern sector of the Shanghai coastal area. As a consequence, present-day archives of SAR images are characterized by a reduced number of scenes with compatible acquisition geometries, and most of them only cover spotted areas of the entire Shanghai district. In addition, a few time gaps, among the different currently-available SAR datasets, are present. To overcome these fundamental limitations, and in order to retrieve a unique displacement time-series (from 2007 to 2016) through combination of available CSK and ASAR/ENVISAT datasets, we developed and applied a proper methodology. The adopted multi-platform combination technique relies on the underlying assumption that, over areas under reclamation, the observed deformations are mostly vertical; moreover, it exploits the knowledge of proper time-dependent geotechnical models [15,19,40–43]. The achieved results are in general agreement with previous studies [43,44], which reported that Lingang New City was characterized, from 2007 to 2010, by annual subsidence rates ranging between 12 and 18 mm/year. They also show that higher deformation rates are measured in regions that are more proximal to the southeastern coast, in correspondence with the reclamation project that was started later.

Therefore, the exploitation of multiple sets of SAR acquisitions, collected in distinct frequency bands, turns out to be helpful for the retrieval of displacement time-series over the entire 2007–2016 time frame, thus allowing us to gain up-to-date insight into the future evolution of the settlement of the ocean-reclaimed platforms.

2. Study Area

The megacity of Shanghai is located at the midpoint of the north–south coastline of China, on the alluvial plain of the Yangtze River Delta. Shanghai is bounded to the north by the Yangtze River estuary, to the east by the East China Sea, and to the south by Hangzhou Bay. The deposits, in most of the city, are soft sediments that were formed during the Quaternary Era [45]. The buried depth of bedrock ranges between 200 and 300 m. The land area of Shanghai covers about 6000 km^2 and is mostly flat, with altitudes ranging between 2 and 6 m above sea level. The city is crossed by the Yangtze River, which is the longest river in Asia, and it is also ranked 4th globally in terms of sediment loads (470 Mt/year) [45].

A significant amount of riverine sediment supply, and the high total riverine sediment discharge rate, in the Yangtze River have made it possible for Shanghai to reclaim land along its eastern coastal areas. As a matter of fact, Shanghai has continuously reclaimed coastal intertidal and wetland areas since the 1950s, in order to build new cities, ports, resorts, and industrial zones. New dikes have

been constructed to trap sediment from the Yangtze River and the coast, in order to make new lands, as evidenced in recent Landsat 8 images (see Figure 1). For ocean-land reclamation, dredging and hydraulic filling methods have been used. Dredger fill, which is a kind of unconsolidated soil with a high water content, large void ratio, and high compressibility, is blown-filled with sludge and dredged out from the coastal seabed [46]. In particular, the reclamation procedure of Lingang New City (see Figure 1) started in 1994, and was almost completed in 2006 [47]. According to the engineering geology characteristics of the area, hydraulic fill soils are composed of two types of alluvial deposits. Dredger fill types, as well as other engineering parameters of the reclamation project, can be found in [48].

3. Data and Methods

3.1. SAR Data

Two independent sets of stripmap SAR images, acquired from different frequency bands, were selected to carry out a comprehensive analysis of the deformation phenomena occurring over the area of Lingang New City (Shanghai). The first dataset is composed of 35 SAR images, collected by the C-band ASAR/ENVISAT sensor [49], from 26 February 2007 to 13 September 2010 (ascending passes, VV polarization, Track 497, Frame 616, swath IS2, with a sensor side-looking and a satellite heading angle of about 23° and 12°, respectively). The second dataset consists of 61 SAR scenes acquired by the SAR sensors of the X-band COSMO-SkyMed (CSK) satellites constellation [50], from 7 December 2013 to 18 March 2016 (descending passes, HH polarization, with a side-looking angle of about 29° and a satellite heading angle of about 8°). As is evident, the two available SAR datasets are not time-overlapping, and there is a long temporal gap (of about three years) between the two relevant groups of images. The distribution of the available SAR images in the temporal/perpendicular baseline plane is also pictorially depicted in Figure 2; the full list of the used SAR data is included in the Supplemental Material.
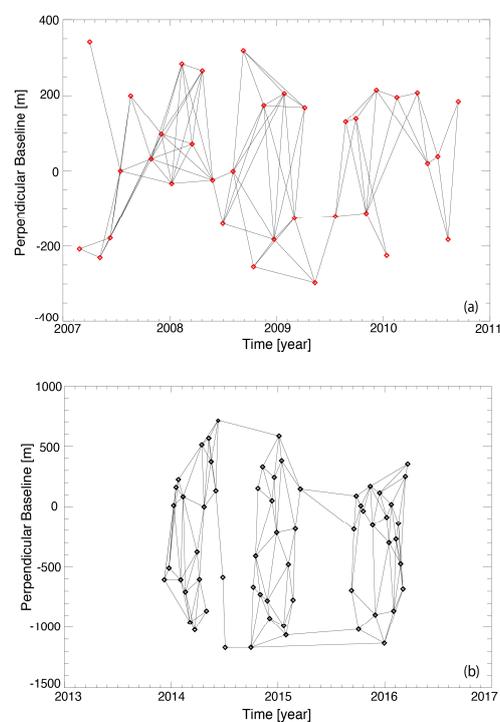

Figure 2. Distribution of the available ASAR/ENVISAT (**a**); and COSMO-SkyMed CSK (**b**) Synthetic Aperture Radar SAR data in the temporal/perpendicular baseline domain; SAR data are represented by **red** (**a**); and **black** (**b**) diamonds, whereas connecting arcs are representative of the selected, small baseline interferometric data pairs.

3.2. The SBAS-DInSAR Technique

Here, we briefly describe the rationale of the SBAS technique. Let us suppose that we have a set of Q co-registered SAR images, acquired at ordered times $[t_1, t_2, \ldots, t_Q]$. Starting from the available data, the SBAS algorithm relies on the proper selection of SAR acquisitions data pairs, characterized by a short temporal (i.e., the time interval between two acquisitions) and spatial (i.e., the distance between two satellite orbits) baseline. The key objective of this data selection is to mitigate the noise (decorrelation) effects [51] that corrupt the interferograms, thus, maximizing the number of temporally coherent SAR pixels (see [52] for the definition of temporal coherence). This baseline selection may imply that SAR data pairs, used to produce differential interferograms, could be arranged in a few SB subsets, which are separated by large baselines. Displacement time-series are then retrieved by solving a least-squares minimization problem, based on the application of the singular value decomposition (SVD) method, to the sequence of unwrapped interferograms. The residual topographic artifacts, as well as the atmospheric phase screen (APS) signals, are also estimated and filtered out. Additional details on the SBAS algorithm, and the SBAS processing chain, can be found in [53,54].

3.3. Vertical Deformation Time-Series Retrieval

After SBAS processing, the LOS displacement time-series are geocoded to a common spatial grid of high-coherent points. For our analysis, let $\mathbf{d}(P) = [d_1(P), d_2(P), \ldots, d_Q(P)]$ be the (geocoded) LOS deformation time-series, which is computed in correspondence with the generic pixel P. Note that the LOS displacement time-series are only known relative to one reference acquisition time, which corresponds to the first SAR acquisition of the available dataset. Accordingly, following [28], we assume $d_1(P) = 0$. Moreover, we also note that the presented method implies a pixel-by-pixel temporal analysis; accordingly, from now on, the dependence of the deformation time-series on pixel P will be not directly mentioned.

LOS deformation values can be expressed as [55–57]:

$$\mathbf{d} = \sin\vartheta\cos\varphi \cdot \mathbf{e} + \sin\vartheta\sin\varphi \cdot \mathbf{n} + \cos\vartheta \cdot \mathbf{h} \tag{1}$$

where $\mathbf{e} = [e_1, e_2, \ldots, e_Q]$, $\mathbf{n} = [n_1, n_2, \ldots, n_Q]$, and $\mathbf{h} = [h_1, h_2, \ldots, h_Q]$ are the 3D cumulative deformation components in the east–west, north–south, and vertical directions, respectively. Moreover, ϑ is the radar side-looking angle, and φ is the corresponding satellite-heading angle. Note that SAR satellite orbits are near polar, circular, and sun-synchronous; accordingly, the sensitivity of the SAR measurements to north–south deformation components (see Equation (1)) is rather limited (i.e., $|\sin\varphi| \ll 1$). Furthermore, if we assume the negligibility of the east–west deformation components, with respect to the vertical ones, the time-series of the vertical deformation components can be derived from the LOS measurements (see Equation (1)) as [19]:

$$\mathbf{h} \cong \frac{\mathbf{d}}{\cos\vartheta} \tag{2}$$

where $h_1 \equiv 0$, since the first image of the considered SAR dataset is assumed to be the temporal reference [28].

3.4. Vertical Deformation Time-Series Combination

The adopted combination scheme is now described. To this end, let us suppose that we have two sets of non-time-overlapped SAR data. The two datasets are composed of Q_1 and Q_2 SAR images, acquired at ordered times $\mathbf{T}_1 = [T_{1,1}, T_{1,2}, \ldots, T_{1,Q_1}]$ and $\mathbf{T}_2 = [T_{2,1}, T_{2,2}, \ldots, T_{2,Q_2}]$, respectively, and $T_{2,1} > T_{1,Q_1}$.

Vertical deformation time-series relevant to homologous highly coherent pixels of the two datasets, namely $\mathbf{h}_1 = [h_{1,1}, h_{1,2}, \ldots, h_{1,Q_1}]$ and $\mathbf{h}_2 = [h_{2,1}, h_{2,2}, \ldots, h_{2,Q_1}]$ (where, taking into account Equation (2), we have $h_{1,1} \equiv 0$ and $h_{2,1} \equiv 0$) are, thus, combined to obtain a unique displacement

time-series, namely $\mathbf{H} = \left[H_1, H_2, \ldots, H_{Q_1+Q_2} \right]$, which spans the overall set of $Q_1 + Q_2$ available SAR acquisition times. All the combined time-series also refer to one global reference time acquisition, which is selected as the time when the oldest SAR image was acquired, namely at time $T_{1,1}$. Accordingly, taking into account that the two sets are not overlapped in time, the combined (unique) vertical deformation time-series vector, $\mathbf{H}$, relevant to the highly coherent pixels, common to both SAR datasets, can be written as:

$$\mathbf{H}\left(\hat{h}\right) = \left[h_{1,1}, h_{1,2}, \ldots, h_{1,Q_1}, h_{2,1} + \hat{h}, h_{2,2} + \hat{h}, \ldots, h_{2,Q_2} + \hat{h} \right] \tag{3}$$

where $\hat{h}$ is the (unknown) vertical deformation at the first time epoch of the second SAR dataset, estimated with respect to the global reference time. Note that the time gap between the SAR datasets makes the use of SVD, as is done in the original SBAS algorithm [28], completely unreliable. To face this problem, we have developed a methodology, which is detailed in what follows.

The fundamental idea is to exploit the knowledge of an external model of the deformation, namely, $\mathbf{m} = \mathbf{m}\left(T, \alpha_1, \alpha_2, \ldots, \alpha_k\right)$, which analytically describes how the deformation is expected to evolve over the entire time, $\mathbf{T} = [\mathbf{T}_1, \mathbf{T}_2]$. The model also depends on the α_i, $i = 1, \ldots, K$ parameters. The best-fit model parameters, as well as the unknown $\hat{h}$ term, are, thus, jointly estimated by solving the following nonlinear optimization problem:

$$\alpha_1, \alpha_2, \ldots, \alpha_k, \hat{h} = \operatorname{argmin} \left[||\mathbf{m} - \mathbf{H}||_2 \right] \tag{4}$$

where the symbol $|| \cdot ||_2$ represents the two-norm of a vector.

We note that the developed algorithm is revealed to be particularly appropriate in the presence of non-linear deformation signals, when other external sources of information of ground displacements are not available, or when the spatial sampling of the measurement points (for instance, derived from Global Positioning System (GPS)/leveling campaigns) is not adequate for linking SAR data. Technical and implementation details of the proposed combination method are detailed in the following section.

4. Experimental Results

In this section, we present the results of the vertical deformation time-series combination, achieved by applying the methodology discussed in Section 3 to two time-gapped C-band ASAR-ENVISAT and X-band CSK SAR datasets.

4.1. SBAS-DInSAR Analysis

We applied the SBAS-DInSAR technique, discussed in Section 3.2, to the available C- and X-band SAR datasets. In particular, we selected SAR data pairs with a perpendicular baseline <800 m and a temporal baseline <400 days; accordingly, we generated $M_1 = 91$ and $M_2 = 155$ interferograms from the ASAR/ENVISAT and the CSK datasets, respectively. For the sake of convenience, the selected SAR data pairs are also represented in the temporal/perpendicular baseline plane of Figure 2a,b, through connecting segments between the SAR data acquisition points. The interferograms were generated by computing the phase difference between the co-registered SAR images pairs [58], and by subtracting the relevant topographic phase contributions, as synthesized using the Shuttle Radar Topography Mission (SRTM) DEM (with a spatial sampling of 90 m × 90 m) of the area [59]. To mitigate the effects of the decorrelation noise, we also independently carried out (on each single interferogram) a complex multilook operation [60] (with 30 looks in the azimuth and range directions for the CSK case, and with 20 looks in the azimuth, and 4 looks in the range direction for the ASAR/ENVISAT case, thus resulting, for both SAR datasets, in a radar pixel dimension of about 90 × 90 m). To each interferogram, a noise-filtering operation [61,62] was also applied. A selection of four interferograms, characterized by different values of the spatial and temporal baselines, is shown in Figure 3. It is

worth noting that the temporal decorrelation noise artifacts corrupt the interferograms as the temporal baseline increases, and this effect is more evident in coastal areas. The generated interferograms were unwrapped using the Extended Minimum Cost Flow (EMCF) algorithm [52]. It is worth noting that phase unwrapping (phU) operations were only involved in the sparse group of coherent pixels common to all the generated interferograms; accordingly, the incoherent areas and the sea have automatically been masked out. Moreover, unwrapped phase signals were calibrated to one selected ground reference point (typically a high coherent pixel), which has been assumed to be motionless [28,63,64]. As is evident, the southeastern sector of the Shanghai megacity looks to be affected more by temporal decorrelation noise artifacts than the highly urbanized city center. This finding is, however, somewhat expected, as coastal areas have changed significantly over time, due to active reclamation processes; in addition, temporal decorrelation is more severe in the X-band than in the C-band [35]. Nevertheless, this does not represent a serious drawback, since DInSAR allows the identification of reliable groups of targets that preserve their coherence [28]. SBAS-DInSAR processing has been exclusively performed on such sparse grids of coherent pixels.
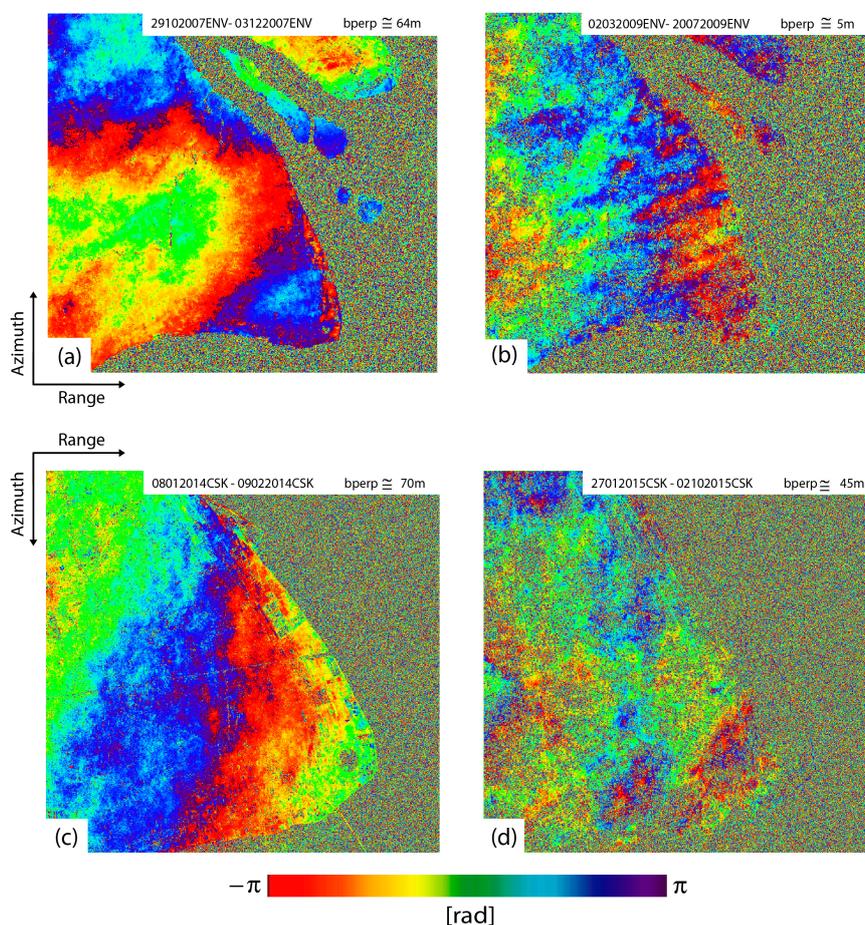

Figure 3. Four selected DInSAR interferograms relevant to the Shanghai area, achieved by exploiting ENVISAT/ASAR acquisitions over ascending orbits (**a**,**b**); and CSK SAR data over descending orbits (**c**,**d**): (**a**) 29 October 2007–3 December 2007, ENVISAT interferogram, with a perpendicular baseline = 64 m, and temporal baseline = 35 days; (**b**) 2 March 2009–20 July 2009, ENVISAT interferogram, with a perpendicular baseline = 5 m, and a temporal baseline = 140 days; (**c**) 8 January 2014–9 February 2014, CSK interferogram, with a perpendicular baseline = 70 m, and a temporal baseline = 32 days; and (**d**) 27 January 2015–2 October 2015, CSK interferogram, with a perpendicular baseline = 45 m, and a temporal baseline = 248 days.

SBAS-DInSAR processing allowed the generation, for both of the two SAR datasets, of a map of the average LOS deformation velocity of the Shanghai area district and, for each coherent pixel, of the corresponding LOS displacement time-series. Maps showing the rates and spatial patterns of surface deformation, observed by both the ASAR/ENVISAT and CSK satellite orbits, are shown in Figure 4a,b, respectively. Displacement maps have been geocoded and superimposed on an amplitude SAR image of the investigated area, and are shown on the grid of coherent pixels that are common to both ASAR/ENVISAT and CSK SAR datasets. Displacements are measured along the satellite LOS: negative velocity values (yellow to red color) represent movements away from the satellite, whereas the blue-green colored pixels are representative of positive velocities. To ensure reliable results, we selected and displayed only coherent SAR pixels, namely, those characterized by a temporal coherence [52] greater than 0.65, and we discarded the low-coherent pixels from the following analyses. We note that temporal coherence [52] is a quality factor of the achieved SBAS-DInSAR LOS deformation time-series, which depends on the noise corrupting interferograms and the phase unwrapping errors that occur during the SBAS processing.
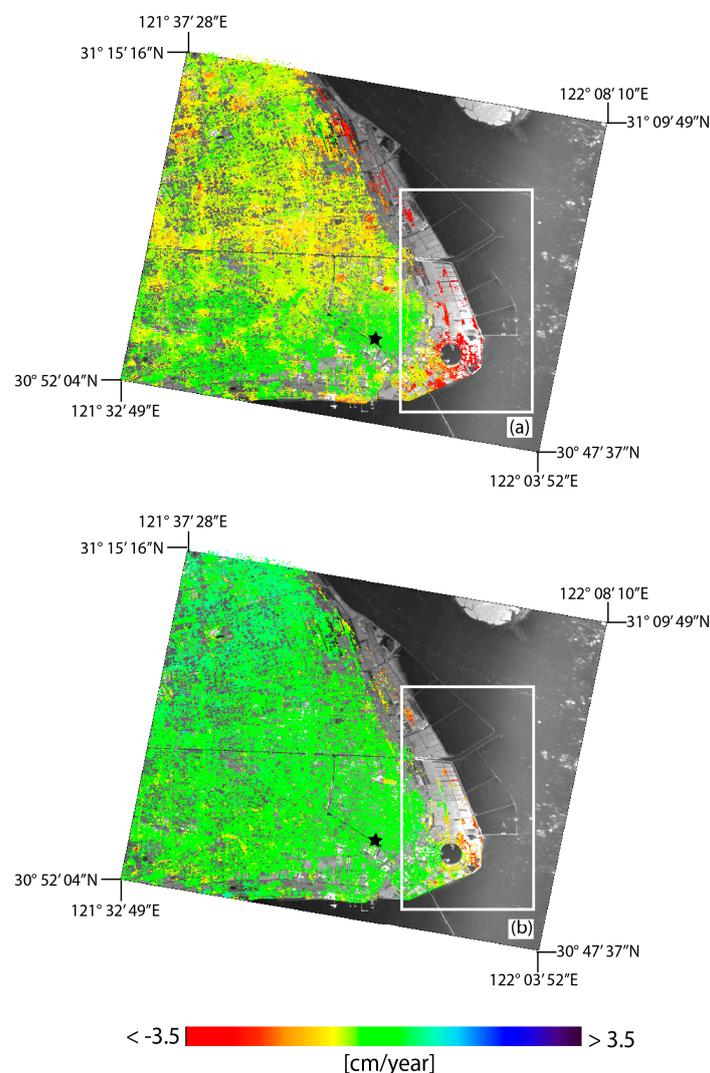

Figure 4. LOS SBAS-DInSAR average displacement velocity maps, retrieved using the 2007–2010 ASAR/ENVISAT (**a**); and the 2014–2016 CSK (**b**) datasets, and shown on a common geocoded grid. The **white** rectangles represent the reclaimed area of Lingang New City, where the following comparative analysis has been performed. The black stars identify the locations of the spatial reference point.

4.2. Combined C-/X-Band Vertical Deformation Time-Series

After the SBAS processing of the two independent ASAR-ENVISAT and CSK datasets, the C-/X-band combination technique, described in Section 3.3, was applied to the two (geocoded) vertical displacement time-series.

For our analyses, we specifically focused on the ocean-reclaimed platforms of Lingang New City (Shanghai), for which a time-dependent geotechnical model of the on-going deformation is available in the literature [40].

More specifically, the adopted time-dependent model, **m**, is provided in [40]:

$$\mathbf{m} = \mathbf{m}\left(\mathbf{T}, S, k, \lambda, \delta\right) = S\frac{\left(\mathbf{T} - \delta\right)^{\lambda}}{k^{\lambda} + \left(\mathbf{T} - \delta\right)^{\lambda}} \tag{5}$$

where **T** represents the vector of the ordered times of all the available SAR acquisitions. Note that, in Equation (5), *S* represents the asymptotic value of vertical deformation (theoretically assumed at time infinite), *k* and λ are two parameters that control the shape of a given curve among the family of all possible curves, and δ is a time-delay, which takes into account the uncertainty of the knowledge of the exact time when reclamation processes ceased, and the self-weight soil consolidation phase started [6]. The model of Equation (5) is recovered from laboratory tests that simulate, at a reduced scale, real scenarios and the kinematic parameters that can be related to dredger-fill soil characteristics (i.e., thickness, water content, void ratio). For additional information, see also [14,42,46]. The combined C-/X-band deformation time-series, spanning the entire time interval covered by the available SAR datasets (from February 2007 to March 2016), were finally retrieved by solving the nonlinear optimization problem in Equation (4) using Equation (5). The problem was efficiently solved through the (iterative) Levenberg–Marquadt least squares (LS) minimization technique [65,66], as provided in the implementation of the MPFIT module, which is available in several programming languages. In particular, for our experiments, we used the code implemented in the MPFIT module, available in the Interactive Data Language (IDL) language environment [67].

As a result, we obtained the combined (vertical) displacement time-series for all the coherent pixels common to both C- and X-band SAR datasets. Figure 5a shows a zoomed view of the map, reporting the mean displacement rate of the vertical deformation in the Lingang New City area, as retrieved by combining ASAR/ENVISAT and CSK data.
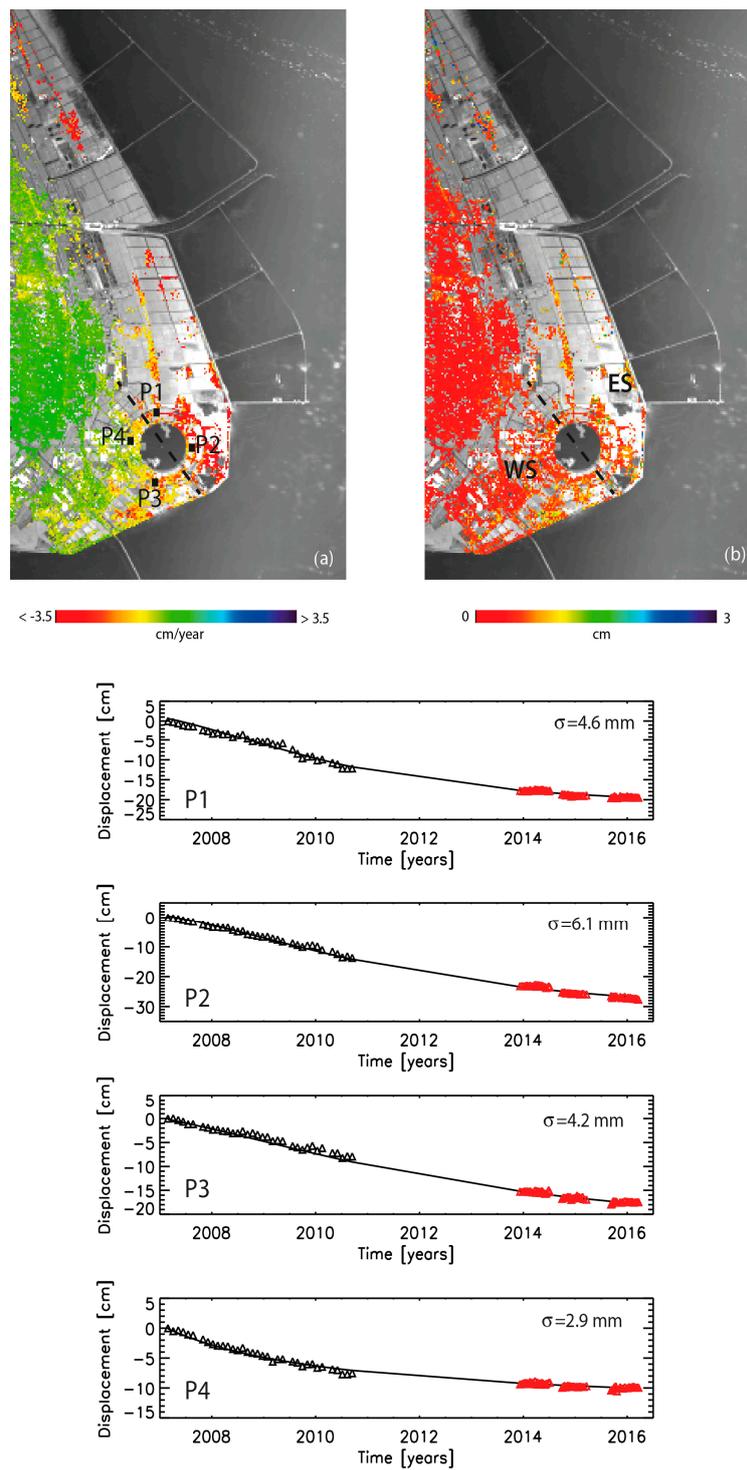
Figure 5. (**a**) Geocoded map of the mean (vertical) deformation velocity during the 2007–2016 time-interval over Lingang New City, as retrieved by combining ENVISAT and CSK LOS displacement time-series; and (**b**) map of the root mean square error (RMSE) values of the difference between the computed best-fit models and the combined ASAR/ENVISAT and CSK (vertical) deformation time-series. The plots of the ENVISAT/CSK combined (vertical) deformation time-series, calculated in correspondence with the four pixels, labeled as P_1, P_2, P_3, and P_4, are also shown. Combined time-series are plotted in **black** (ASAR/ENVISAT) and **red** (CSK) triangles, whereas the corresponding best-fit models are plotted by continuous **black** lines.

5. Discussion

In this section, we discuss the combined SBAS-DInSAR results, taking into account the characteristics of the deformation signals retrieved from the ocean-reclaimed platforms of Shanghai.

First, we focus on the detected deformation signals, and we discuss the assumption of negligibility of the east–west component of the surface displacements with respect to the vertical (subsidence/uplift) one. We note that such an assumption is valid in ocean-reclaimed platforms, but it is not true of the overall Shanghai megacity area. Indeed, the southwestern sector of the Shanghai area has recently been claimed to be crossed by a geological fault, the so-called Dachang–Zhoupu fault (see black line in Figure 1). The fault is responsible for appreciable east–west deformation movements in that sector of the city (with a magnitude, however, less than 1 cm/year, with respect to a reference point located in correspondence with the GPS station labeled as SHAO in Figure 1). Such displacements were measured in the 2002–2005 period, through a network of 17 GPS stations (see [68] for the locations of the GPS stations, and their relative movements), and were related to the neotectonic activity of an existing geological fault [68,69]. Nevertheless, there is no direct evidence that these east–west deformations also extend to the reclaimed areas, located southeast of Shanghai, where it is known that the deformations are dominated by soil compaction mechanisms, which are primarily responsible for vertical movements. For this reason, the additional contributions to settlement, due to fault mechanisms, have been assumed to be negligible in our study.

We note that, despite the fact that ASAR/ENVISAT and CSK data have been acquired through ascending and descending passes, they cannot be combined to extrapolate the east–west and vertical (up–down) components of deformations, as they do not span the same period of observation. Furthermore, it is worth highlighting that, for Lingang New City, the deformation is mostly non-linear in time, thus, the simple option to extrapolate a linear rate from ASAR/ENVISAT time series, and to use that value for linking ASAR/ENVISAT and CSK vertical deformation time-series, appears to be unreliable. With respect to the used model in Equation (5), we note that it is derived from laboratory tests aimed at assessing, for instance, the stability and capacity of building foundations. Its fundamental principle is to recreate the conditions that would exist in a full-scale construction by using a model on a reduced scale. Centrifuge model testing provides researchers with simulated data that can improve the understanding of the underlying mechanisms of deformation, allowing the retrieval of experimental data for the verification of numerical models. Of particular interest, due to the peculiar alluvial soil characteristics of Shanghai, is the settlement model found in [40], which permits to analyze ground settlements caused primarily by self-weight consolidation mechanisms. The simplified model in [40] can be derived from the general model described in [46], and those presented in [14], which relate kinematic parameters to soil physical characteristics.

At this stage, we discuss the achieved results, by specifically focusing on the ocean-reclaimed area of Lingang New City. As mentioned earlier, the multi-platform time-series combination was performed by searching for the model parameters, as well as the (unknown) bias between the ASAR/ENVISAT and the CSK time-series that best fit the data. Subsequently, we also checked the quality of the nonlinear curve fitting, by calculating the root mean square error (RMSE) of the difference between the (reconstructed) DInSAR-based (vertical) deformation time-series and the obtained best-fit model. The map of the RMSE values is shown in Figure 5b. Looking at Figure 5b, it is evident that the obtained RMSE is, on average, on the order of a few millimeters. Table 1 also reports the average RMSE values calculated over the areas of Lingang New City in its western (WS) and eastern (ES) sectors, respectively, as retrieved from the combined ASAR/ENVISAT and CSK (vertical) deformation time-series. In addition, we repeated the RMSE calculation by separately considering the fitting of the obtained models and the ASAR/ENVISAT and CSK time-series. The achieved results are also summarized in Table 1.

Table 1. Average root mean square error (RMSE) values between the DInSAR time-series and the recovered best-fit models for the western (WS) and the eastern (ES) sectors.

Sensor	WS (mm)	ES (mm)
ENVISAT	5.8	8.0
CSK	3.4	5.7
ENVISAT/CSK	4.8	7.2

We note that the best-fit models retrieved as the result of the combination of C/X-band displacement time-series are in general agreement with the forecast models studied in our previous investigation [19], which were exclusively based on the use of ASAR/ENVISAT data. Moreover, it is worth noting that the new CSK deformation time-series distinctly show that the rate of deformation in ocean-reclaimed platforms has been progressively decreasing over the most recent six years, which is in general accordance with the time-dependency of the models in Equation (5). This is also confirmed by the temporal shape of the individual ASAR/ENVISAT and the CSK time-series, as well as by the plots of the combined (vertical) deformation time-series. In particular, Figure 5 shows the deformation time-series relevant to the four selected pixels, labeled as P_1, P_2, P_3, and P_4. Table 2 lists the best-fit model parameters retrieved for these four selected points. We note that these pixels have been selected among the ones characterized by the smallest RMSE values (which are indicated for all the four pixels in the plots of Figure 5) as being representative of the (average) present-state of residual settlements in the different zones of Lingang New City.

Table 2. Values of the best-fit model parameters retrieved for the four selected points of Figure 5b.

Point	S (cm)	k	λ	δ
P1	−19.7	11.9	0.7	−5
P2	−41.2	26.6	0.7	−3
P3	−27.6	16.2	0.7	−1
P4	−11.4	8.6	0.5	−4

As shown in previous investigations, it is clear that the eastern part of the city is still (in 2016) affected by appreciable deformations. Conversely, the western sector of the city is, at present, ten years after the end of the reclamation processes [19], almost stable. One of the outcomes of our previous investigation was the recovery of some preliminary predictions of the cumulative displacements in the ocean-reclaimed platforms of Shanghai by the end of 2015, 2020, and 2025 (see Figure 8 of [19]), calculated by considering the end of reclamation procedures as the starting time for the soil consolidation phase. Finally, we also estimated the deviation between the (average) measured and modeled deformation rates for both the ES and WS of the city in the 2007–2010 and 2014–2016 observation periods, respectively. The achieved results are summarized in Table 3. In the analysis, there is a perfect agreement between the measured and the modeled deformation (subsidence) rates in the 2007–2010 period. Conversely, in the 2014–2016 period, the agreement is perfect in the WS, whereas there is an average difference of about 3 mm/year in the ES. This finding is not surprising, being that the soil consolidation stages in the ES of the city have not yet concluded.

Table 3. Average rates of deformation in the eastern and western sector in the two 2007–2010 and 2014–2016 time intervals.

Period	Measured (mm/Year)		Modeled (mm/Year)	
	WS	ES	WS	ES
2007–2010	−16.9	−35.0	−16.6	−35.2
2014–2016	−3.9	−16.9	−3.4	−13.4

One goal of the present analysis is to confirm/corroborate our previous results, taking into account the shape of the (vertical) deformation time-series in recent years (2013–2016), as captured by the CSK constellation sensors. As a matter of fact, the comparison between the predicted cumulative displacement maps related to 2015 and the one obtained in March 2016 (see Figure 6) shows that the newly acquired CSK data chiefly confirm the validity of previous best-fit models (see Figure 8 of [19] for a direct comparison). The deviation of the measured deformations from best-fit models, as retrieved using only ASAR/ENVISAT data (covering the period from 2007 to 2010), and the ones recovered using the combined ASAR/ENVISAT and CSK data, is minimal, as testified by the average RMSE values listed in Table 4. The differences between the newly derived model and the old models are more appreciable in the eastern sector of the city than those in the western sector. This is due to the different types of soils used and the various stages of soil consolidation that the two areas experience.
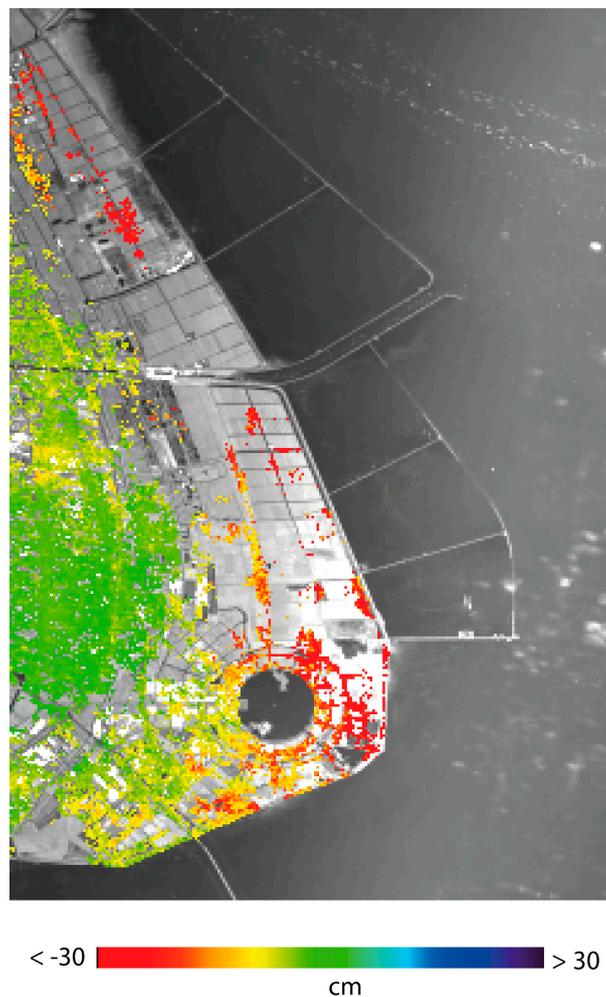

Figure 6. Map of the entire cumulative displacements on 18 March 2016, as obtained by the combination of ASAR/ENVISAT and the CSK time-series.

Table 4. Average RMSE values of the differences between the best-fit models retrieved by using only ENVISAT data (2007–2010) and the ones extracted from the combined ENVISAT/CSK data (2007–2016). RMSE values are computed for both the western and the eastern sectors of Lingang New City.

Sensor	WS	ES
ENVISAT vs. ENVISAT/CSK	3.9 mm	6.4 mm

6. Conclusions

An up-to-date investigation of the residual deformations of ocean-reclaimed platforms over the coastal area of the Shanghai megacity, as recovered by appropriately combining DInSAR-driven time-series of deformation, obtained from the different (C- and X-) frequency bands, is provided in this work. In particular, we processed ASAR/ENVISAT (C-band) and CSK (X-band) radar images, acquired from 2007 to 2016. The achieved DInSAR deformation time-series were then jointly integrated by making use of the time-dependent geotechnical model, derived from laboratory centrifuge tests, regarding the deformations occurring in the area under investigation. In particular, in this work, we used such models to further extend some previous analyses [19]. As a result, we show that there is a good agreement between the combined-C/X-band DInSAR (vertical) time-series, and what is theoretically expected from the model. The newly-processed CSK time-series show that the deformation rate in ocean-reclaimed platforms has generally been reducing over time, in both the western and eastern sectors. In particular, the areas that were firstly reclaimed in the WS are today (almost ten years after the end of reclamation procedures) rather stable (i.e., the deformation rate is approaching zero). On the other hand, the ES zone, where the reclamation processes started later, is still affected by significant deformation signals, with deformation rates on the order of 15 mm/year.

The method we used to link time-gapped displacement time-series relies on the knowledge of a model for the expected deformation, and the hypothesis that deformation over reclaimed platforms is mostly vertical. The latter assumption is reasonable, as the soil consolidation stages, as well as the mechanisms induced by the weight of the buildings, which have been built in the new city, are, at most, responsible for vertical movements of the terrain. Nevertheless, the lack of sufficiently large archives of time-overlapped ascending/descending SAR images over Lingang New City (with respect to the reclaimed areas) makes the measurement of the east–west deformation rates directly from SAR data unreliable, as shown, for instance, by using the methods in [55,70–75]. Moreover, such a strategy can be extended to other cases where deformation components in east–west directions cannot be considered negligible. This can be done by effectively combining the strategies adopted here, and the combination methods discussed in [55,70–75], which exploit SAR data acquired by multiple sensors and different orbital positions (e.g., from ascending and descending passages). In addition, the adopted combination scheme can be further generalized to the point where more than two time-gapped sequences of SAR images are available.

To extend, and fully validate, our prediction models, we count on gaining access, in the near future, to data gathered by a network of GPS that are currently being deployed in Lingang New City, and to make use of the archives of newly-acquired SAR data collected by the European Sentinel-1A/-1B C-band SAR sensors of the Copernicus program [76]. In fact, at the time of this investigation, Sentinel-1 archives relevant to the area under investigation were not sufficiently populated (less than 20 scenes) to allow the generation of reliable and steady displacement time-series. Their use is a matter for further studies.

Supplementary Materials: The following are available online at www.mdpi.com/2072-4292/8/11/911/s1. Table S1: ASAR/ENVISAT SAR Acquisition list. Table S2: CSK SAR Acquisition list.

Author Contributions: Antonio Pepe developed the combination method and supervised the research and the algorithm development; he also prepared the manuscript. Manuela Bonano computed the ASAR/ENVISAT and the CSK DInSAR time-series and revised the manuscript. Qing Zhao contributed to the preparation of the manuscript and provided information for the geophysical assessment of the area. Tianliang Yang and Hamei Wang revised the manuscript and searched the recent literature related to the area under investigation.

Conflicts of Interest: The authors declare no conflicts of interest.

References

1. Hoeksema, R.J. Three stages in the history of land reclamation in the Netherlands. *Irrig. Drain.* **2007**, *56*, 113–216. [CrossRef]
2. Douglas, I.; Lawson, N. Airport construction: Materials use and geomorphic change. *J. Air Trans. Manag.* **2003**, *9*, 177–185. [CrossRef]
3. Zhao, Q.; Lin, H.; Gao, W.; Zebker, H.; Chen, A.; Yeung, K. InSAR detection of residual settlement of an ocean reclamation engineering project: A case study of Hong Kong International Airport. *J. Oceanogr.* **2011**, *67*, 415–426. [CrossRef]
4. Ganesalingam, D.; Ameratunga, J.; Scweitzer, G.; Boyle, P.; Sivakugan, S. Anisotropy in the permeability and consolidation characteristics of dredged mud. In Proceedings of the ANZ 2012, Ground Engineering in a Changing World: 11th Australia–New Zealand Conference on Geomechanics, Melbourne, Australia, 15–18 July 2012; pp. 752–757.
5. Philip, D.R.E.; McIlquham, J.D. Geotechnical design for the Port Botany expansion project. *Proc. Inst. Civ. Eng. Geotech. Eng.* **2011**, *164*, 149–167.
6. Puzrin, A.M.; Alonso, E.E.; Pinyol, N.M. Unexpected Excessive Settlements: Kansai International Airport, Japan. In *Geomechanics of Failures*; Springer: New York, NY, USA, 2010; pp. 23–43.
7. Rizzo, A. Metro Doha. *Cities* **2013**, *31*, 533–543. [CrossRef]
8. Yang, H. Legal Regulation of Land Reclamation in China's Coastal Area. *Coast. Manag.* **2014**, *42*, 9–79.
9. Yin, Y.H. Thinking on large area reclamation in Caofeidian, Tangshan city, Hebei Province. *Mar. Geol. Lett.* **2007**, *23*, 1–10.
10. Wang, Z.Y.; Li, Y.; He, Y. Sediment budget of the Yangtze River. *Water Resour. Res.* **2007**, *43*, 1–14. [CrossRef]
11. Liu, G.X.; Luo, X.J.; Chen, Q.; Huang, J.F.; Ding, X.L. Detecting land subsidence in Shanghai by PS-networking SAR interferometry. *Sensors* **2008**, *8*, 4725–4741. [CrossRef]
12. Bhattacharyaa, S.; Hyodob, M.; Godaa, K.; Tazohc, T.; Taylora, C.A. Liquefaction of soil in the Tokyo Bay area from the 2011 Tohoku (Japan) earthquake. *Soil Dyn. Earthq. Eng.* **2011**, *31*, 1618–1628. [CrossRef]
13. Chien, L.K.; Oh, Y.N.; Chang, C.H. Effects of fines content on liquefaction strength and dynamic settlement of reclaimed soil. *Can. Geotech. J.* **2002**, *39*, 254–265. [CrossRef]
14. Plant, G.W.; Covil, C.S.; Hughes, R.A. Geology, Surveying, Reclamation Settlement. In *Site Preparation of the New Hong Kong International Airport*, 1st ed.; Thomas Telford: London, UK, 1998.
15. Yang, M.S.; Jiang, Y.; Liao, M.; Wang, H. The analysis of the subsidence patterns in Lingang New City (Shanghai) using high-resolution SAR images. *Shanghai Land Resour.* **2013**, *34*, 12–16. (In Chinese)
16. Chen, J.; Wu, J.; Zhang, L.; Zou, J.; Liu, G.; Zhang, R.; Yu, B. Deformation Trend Extraction Based on Multi-Temporal InSAR in Shanghai. *Remote Sens.* **2013**, *5*, 1774–1786. [CrossRef]
17. Perissin, D.; Wang, Z.; Lin, H. Shanghai subway tunnels and highways monitoring through Cosmo-SkyMed Persistent Scatterers. *ISPRS J. Photogramm. Remote Sens.* **2012**, *73*, 58–67. [CrossRef]
18. Dong, S.; Samsonov, S.; Yin, H.; Ye, S.; Cao, Y. Time-series analysis of subsidence associated with rapid urbanization in Shanghai, China measured with SBAS InSAR method. *Environ. Earth Sci.* **2014**, *72*, 677–691. [CrossRef]
19. Zhao, Q.; Pepe, A.; Gao, W.; Lu, Z.; Bonano, M.; He, M.L.; Wang, J.; Tang, X. A DInSAR Investigation of the Ground Settlement Time Evolution of Ocean-Reclaimed Lands in Shanghai. *IEEE Sel. Top. Appl. Earth Obs. Remote Sens.* **2015**, *8*, 1763–1781. [CrossRef]
20. Been, K.; Sills, G.C. Self-weight consolidation of soft soils: An experimental and theoretical study. *Geotechnique* **1981**, *31*, 519–535. [CrossRef]
21. Terzaghi, K.; Ralph, P.B.; Gholamreza, M. *Soil Mechanics in Engineering Practice*, 3rd ed.; Wiley-Interscience: Hoboken, NJ, USA, 1996; pp. 1–592.

22. Bürgmann, R.; Rosen, P.A.; Fielding, E.J. Synthetic aperture radar interferometry to measure Earth's surface topography and its deformation. *Annu. Rev. Earth Planet. Sci.* **2000**, *28*, 169–209. [CrossRef]

23. Massonnet, D.; Feigl, K.L. Radar interferometry and its application to changes in the Earth's surface. *Rev. Geophys.* **1998**, *36*, 441–500. [CrossRef]

24. Massonnet, D.; Rossi, M.; Carmona, C.; Adragna, F.; Peltzer, G.; Feigl, K.; Rabaute, T. The displacement field of the Landers earthquake mapped by radar interferometry. *Nature* **1993**, *364*, 138–142. [CrossRef]

25. Massonnet, D.; Briole, P.; Arnaud, A. Deflation of Mount Etna monitored by spaceborne radar interferometry. *Nature* **1995**, *375*, 567–570. [CrossRef]

26. Ferretti, A.; Prati, C.; Rocca, F. Permanent scatterers in SAR interferometry. *IEEE Trans. Geosci. Remote Sens.* **2001**, *39*, 8–20. [CrossRef]

27. Kampes, B.M. *Radar Interferometry: Persistent Scatterer Technique*; Springer: New York, NY, USA, 2006.

28. Berardino, P.; Fornaro, G.; Lanari, R.; Sansosti, E. A new algorithm for surface deformation monitoring based on small baseline differential SAR interferograms. *IEEE Trans. Geosci. Remote Sens.* **2004**, *40*, 2375–2383. [CrossRef]

29. Mora, O.; Mallorquí, J.J.; Broquetas, A. Linear and nonlinear terrain deformation maps from a reduced set of interferometric SAR images. *IEEE Trans. Geosci. Remote Sens.* **2003**, *41*, 2243–2253. [CrossRef]

30. Usai, S. A least squares database approach for SAR interferometric data. *IEEE Trans. Geosci. Remote Sens.* **2003**, *41*, 753–760. [CrossRef]

31. Hooper, A.; Bekaert, D.; Spaans, K.; Arıkan, M. Recent advances in SAR interferometry time series analysis for measuring crustal deformation. *Tectonophysics* **2012**, *514*, 1–13. [CrossRef]

32. Strang, G. *Linear Algebra and Its Appications*; Harcourt Brace Jovanovich: Orlando, FL, USA, 1988.

33. Greif, V.; Vicko, J. Monitoring of post-failure landslide deformation by the PS-InSAR technique at Lubietova in Central Slovakia. *Environ. Earth Sci.* **2012**, *66*, 1585–1595. [CrossRef]

34. Guzzetti, F.; Manunta, M.; Ardizzone, F.; Pepe, A.; Cardinali, M.; Zeni, G.; Reichenbach, P.; Lanari, R. Analysis of ground deformation detected using the SBAS-DInSAR technique in Umbria, Central Italy. *Pure Appl. Geophys.* **2009**, *166*. [CrossRef]

35. Bonano, M.; Manunta, M.; Pepe, A.; Paglia, L.; Lanari, R. From previous C-band to New X-band SAR systems: Assessment of the DInSAR mapping improvement for deformation time-series retrieval in urban areas. *IEEE Trans. Geosci. Remote Sens.* **2013**, *51*, 1973–1984. [CrossRef]

36. Parcharidis, I.; Lagios, E.; Sakkas, V.; Raucoules, D.; Feurer, D.; le Mouelic, S.; King, C.; Carnec, C.; Novali, F.; Ferretti, A.; et al. Subsidence monitoring within the Athens Basin (Greece) using space radar interferometric techniques. *Earth Planets Space* **2006**, *58*, 505–513. [CrossRef]

37. Cavalie, O.; Sladen, A.; Kelner, M. Detailed quantification of delta subsidence, compaction and interaction with man-made structures: The case of the NCA airport, France. *Nat. Hazards Earth Syst. Sci.* **2015**, *9*, 1973–1984. [CrossRef]

38. Zhang, J.Z.; Hauang, H.; Bi, H. Land Subsidence in the modern Yellow River Delta based on InSAR time-series Analysis. *Nat. Hazards* **2015**, *75*, 2385–2397. [CrossRef]

39. Aly, M.H.; Klein, A.G.; Zebker, H. Land Subsidence in the Nile Delta of Egypt by persistent scatterer interferometry. *Remote Sens. Lett.* **2012**, *3*, 621–630. [CrossRef]

40. Yang, P.; Tang, Y.Q.; Zhou, N.Q.; Wang, J.X. Consolidation settlement of Shanghai dredger fill under self-weight using centrifuge modeling test. *J. Cent. South Univ. Technol.* **2008**, *39*, 862–866. (In Chinese)

41. Taylor, R.N. *Geothecnical Centrifuge Technology*; Blackie Academic and Professional: Glasgow, UK, 1995.

42. Cui, Z.D.; Tang, Y.Q. Land subsidence and pore structure of soils caused by the high-rise building group through centrifuge model test. *Eng. Geol.* **2010**, *113*, 44–52. [CrossRef]

43. Xu, Y.S.; Ma, L.; Du, Y.J.; Shen, S.L. Analysis of urbanization-induced land subsidence in Shanghai. *Nat. Hazards* **2012**, *63*, 1255–1267. [CrossRef]

44. Shanghai Municipal Bureau of Planning and Land Resources. *Shanghai Geological Environmental Bulletin (2001–2009)*; Shanghai Municipal Bureau of Planning and Land Resources: Shanghai, China, 2009. (In Chinese)

45. Yang, S.L.; Milliman, J.D.; Li, P.; Xu, K. 50,000 dams later: Erosion of the Yangtze River and its delta. *Glob. Planet. Chang.* **2011**, *75*, 14–20. [CrossRef]

46. Tang, Y.; Zhou, J.; He, X.; Yang, P.; Wang, J. Theoretical and experimental study of consolidation settlement characteristics of hydraulic fill soil in Shanghai. *Environ. Earth Sci.* **2012**, *67*, 1397–1405. [CrossRef]

47. Shen, S.L. Geological environmental character of Lin Gang New City and its influences to the construction. *Shanghai Geol.* **2008**, *105*, 24–28. (In Chinese)

48. Shi, Y.; Yan, X.; Zhou, N. Land subsidence induced by recent alluvia deposits in Yangtze River delta area, a case study of Shanghai Lingang New City. *J. Eng. Geol.* **2007**, *15*, 391–402. (In Chinese)

49. Desnos, Y.L.; Laur, H.; Lim, P.; Meisl, P.; Gach, T. The Envisat-1 advanced synthetic aperture radar processor and data products. In Proceedings of the IEEE 1999 International Geoscience and Remote Sensing Symposium, Hamburg, Germany, 28 June–2 July 1999; pp. 1683–1685.

50. Covello, F.; Battazza, F.; Coletta, A.; Lopinto, E.; Fiorentino, C.; Pietranera, L.; Valentini, G.; Zoffoli, S. COSMO-SkyMed an existing opportunity for observing the Earth. *J. Geodyn.* **2010**, *49*, 171–180. [CrossRef]

51. Zebker, H.A.; Villasenor, J. Decorrelation in interferometric radar echoes. *IEEE Trans. Geosci. Remote Sens.* **1992**, *30*, 950–959. [CrossRef]

52. Pepe, A.; Lanari, R. On the extension of the minimum cost flow algorithm for phase unwrapping of multitemporal differential SAR interferograms. *IEEE Trans. Geosci. Remote Sens.* **2006**, *44*, 2374–2383. [CrossRef]

53. Lanari, R.; Casu, F.; Manzo, M.; Zeni, G.; Berardino, P.; Manunta, M.; Pepe, A. An overview of the small BAseline subset algorithm: A DInSAR technique for surface deformation analysis. *Pure Appl. Geophys.* **2007**, *164*, 637–661. [CrossRef]

54. Manzo, M.; Fialko, Y.; Casu, F.; Pepe, A.; Lanari, R. A quantitative assessment of DInSAR measurements of interseismic deformation: The Southern San Andreas fault case study. *Pure Appl. Geophys.* **2012**, *169*, 1463–1482. [CrossRef]

55. Fialko, Y.; Simons, M.; Agnew, D. The complete (3-D) surface displacement field in the epicentral area of the 1999 M(w)7.1 Hector Mine earthquake, California, from space geodetic observations. *Geophys. Res. Lett.* **2001**, *28*, 3063–3066. [CrossRef]

56. Wright, T.J.; Parsons, B.E.; Lu, Z. Toward mapping surface deformation in three dimensions using InSAR. *Geophys. Res. Lett.* **2004**, *31*, L01607. [CrossRef]

57. Gray, L. Using multiple RADARSAT InSAR pairs to estimate a full three-dimensional solution for glacial ice movement. *Geophys. Res. Lett.* **2011**, *38*, L05502-1–L05502-6. [CrossRef]

58. Sansosti, E.; Berardino, P.; Manunta, M.; Serafino, F.; Fornaro, G. Geometrical SAR image registration. *IEEE Trans. Geosci. Remote Sens.* **2006**, *44*, 2861–2870. [CrossRef]

59. Rosen, P.A.; Hensley, S.; Gurrola, E.; Rogez, F.; Chan, S.; Martin, J. SRTM C-band topographic data quality assessment and calibration activities. In Proceedings of the IEEE 2001 International Geoscience and Remote Sensing Symposium, Sydney, Australia, 9–13 July 2001; pp. 739–741.

60. Rosen, P.A.; Hensley, S.; Joughin, I.R.; Li, F.K.; Madsen, S.N.; Rodriguez, E.; Goldstein, R.M. Synthetic aperture radar interferometry. *IEEE Trans. Geosci. Remote Sens.* **2000**, *48*, 333–382. [CrossRef]

61. Goldstein, R.M.; Werner, C.L. Radar interferogram filtering for geophysical applications. *Geophys. Res. Lett.* **1998**, *25*, 4035–4038. [CrossRef]

62. Yang, Y.; Pepe, A.; Manzo, M.; Bonano, M.; Liang, D.N.; Lanari, R. A simple Solution to Mitigate Noise Effects in Time-Redundant Sequences of Small Baseline Multi-look DInSAR Interferograms. *Remote Sens. Lett.* **2013**, *4*, 609–618.

63. Wang, T.; Liao, M.; Perissin, D. InSAR coherence-decomposition analysis. *IEEE Geosci. Remote Sens. Lett.* **2010**, *7*, 156–160. [CrossRef]

64. Navarro-Sanchez, V.D.; Lopez-Sanchez, J.M.; Vicente-Guijalba, F. A contribution of polarimetry to satellite differential SAR interferometry: Increasing the number of pixel candidates. *IEEE Geosci. Remote Sens. Lett.* **2010**, *7*, 276–280. [CrossRef]

65. Levenberg, K. A Method for the Solution of Certain Non-Linear Problems in Least Squares. *Q. Appl. Math.* **1994**, *2*, 164–168.

66. Marquardt, D. An Algorithm for Least-Squares Estimation of Nonlinear Parameters. *SIAM J. Appl. Math.* **1963**, *11*, 431–441. [CrossRef]

67. Markwardt, C.B. Non-linear Least Squares Fitting in IDL with MPFIT. In Proceedings of the 17th Annual Conference on Astronomical Data Analysis Software and Systems (ADASS XVII), London, UK, 23–26 September 2007.

68. Cai, J.; Wang, J.; Wu, J.; Hu, C.; Grafarend, E.; Chen, J. Horizontal deformation rate analysis based on multiepoch GPS measurements in Shanghai. *J. Surv. Eng.* **2008**, *134*, 132–137. [CrossRef]

69. Dai, K.; Liu, G.; Li, Z.; Li, T.; Yu, B.; Wang, X.; Singleton, A. Extracting Vertical Displacement Rates in Shanghai (China) with Multi-Platform SAR Images. *Remote Sens.* **2015**, *7*, 9542–9562. [CrossRef]

70. Shirzaei, M. A seamless multitrack multitemporal InSAR algorithm. *Geochem. Geophys. Geosyst.* **2015**, *16*, 1656–1669. [CrossRef]

71. Hu, J.; Ding, X.; Li, Z.; Zhu, J.; Sun, Q.; Zhang, L. Kalman-Filter-Based Approach for Multisensor, Multitrack, and Multitemporal InSAR. *IEEE Trans. Geosci. Remote Sens.* **2013**, *51*, 4226–4239. [CrossRef]

72. Manzo, M.; Ricciardi, G.P.; Casu, F.; Ventura, G.; Zeni, G.; Borgstrom, S.; Berardino, P.; del Gaudio, C.; Lanari, R. Surface deformation analysis in the Ischia Island (Italy) based on spaceborne radar interferometry. *J. Volcanol. Geotherm. Res.* **2006**, *151*, 399–416. [CrossRef]

73. Gourmelen, N.; Amelung, F.; Casu, F.; Manzo, M.; Lanari, R. Mining-related ground deformation in Crescent Valley, Nevada: Implications for sparse GPS networks. *Geophys. Res. Lett.* **2007**, *34*, L09309. [CrossRef]

74. Samsonov, S.; d'Oreye, N. Multidimensional time-series analysis of ground deformation from multiple InSAR data sets applied to Virunga Volcanic Province. *Geophys. J. Int.* **2012**, *191*, 1095–1108.

75. Pepe, A.; Solaro, G.; Calò, F.; Dema, C. A Minimum-Acceleration Approach for the Retrieval of Multi-Platform InSAR Deformation Time-Series. *IEEE J. Sel. Top. Appl. Earth Obs. Remote Sens.* **2016**, in press. [CrossRef]

76. Torres, R.; Snoeij, P.; Geudtner, D.; Bibby, D.; Davidson, M.; Attema, E.; Potin, P.; Rommen, B.; Floury, N.; Brown, M.; et al. GMES Sentinel-1 mission. *Remote Sens. Environ.* **2012**, *120*, 9–24. [CrossRef]